© 2016. Published by The Company of Biologists Ltd | Development (2016) 143, 1126-1133 doi:10.1242/dev.131516

RESEARCH ARTICLE

Mutations in the murine homologue of *TUBB5* cause microcephaly by perturbing cell cycle progression and inducing p53-associated apoptosis

Martin Breuss[1], Tanja Fritz[1], Thomas Gstrein[1], Kelvin Chan[1,2], Lyubov Ushakova[1], Nuo Yu[1], Frederick W. Vonberg[1,3], Barbara Werner[1], Ulrich Elling[4] and David A. Keays[1,*]

ABSTRACT

Microtubules play a crucial role in the generation, migration and differentiation of nascent neurons in the developing vertebrate brain. Mutations in the constituents of microtubules, the tubulins, are known to cause an array of neurological disorders, including lissencephaly, polymicrogyria and microcephaly. In this study we explore the genetic and cellular mechanisms that cause TUBB5-associated microcephaly by exploiting two new mouse models: a conditional E401K knock-in, and a conditional knockout animal. These mice present with profound microcephaly due to a loss of upper-layer neurons that correlates with massive apoptosis and upregulation of p53. This phenotype is associated with a delay in cell cycle progression and ectopic DNA elements in progenitors, which is dependent on the dosage of functional Tubb5. Strikingly, we report ectopic Sox2-positive progenitors and defects in spindle orientation in our knock-in mouse line, which are absent in knockout animals. This work sheds light on the functional repertoire of Tubb5, reveals that the E401K mutation acts by a complex mechanism, and demonstrates that the cellular pathology driving *TUBB5*-associated microcephaly is cell death.

KEY WORDS: Microcephaly, Tubulin, Apoptosis, Trp53

INTRODUCTION

The generation of the mammalian neocortex relies on a functional microtubule cytoskeleton (Ayala et al., 2007; Kuijpers and Hoogenraad, 2011). Microtubules mediate the separation of sister chromatids in neuronal progenitors, translocate the nucleus in postmitotic migrating neurons, and enable axonal elongation, connecting disparate brain regions (Dent et al., 2011; Dickson, 2002). Mutations in the tubulin genes (*TUBA1A*, *TUBB2A*, *TUBB2B*, *TUBB3*, *TUBB5*, *TUBA4A*, *TUBB4A*, *TUBG1*) have been implicated in a variety of human neurological diseases, now referred to as the tubulinopathies (Bahi-Buisson et al., 2014; Breuss and Keays, 2014; Smith et al., 2014). These disorders include lissencephaly, polymicrogyria, amyotrophic lateral sclerosis, and ocular motility disorders (Jaglin et al., 2012; Smith et al., 2014; Tischfield et al., 2011).

We have recently reported that mutations in the beta-tubulin isoform *TUBB5* can cause microcephaly with structural brain abnormalities (Breuss et al., 2012; Ngo et al., 2014). *Tubb5* is widely expressed throughout embryonic development, and is enriched in the developing cortex, where it is found in radial glial progenitors, intermediate progenitors and postmitotic neurons. As is true for the vast majority of tubulin mutations that cause human disease, those in *TUBB5* are heterozygous and *de novo*. The preponderance of such mutations and absence of disease-causing null alleles has led to the assertion that tubulin mutations act by a gain-of-function mechanism rather than haploinsufficiency (Hu et al., 2014; Kumar et al., 2010).

Here, we investigate this contention by generating an E401K conditional knock-in and a conditional knockout line. The E401K mouse line recapitulates a mutation found in a patient who presented with severe microcephaly (–4SD), partial agenesis of the corpus callosum, but with an intact cortical architecture. We show that our *Tubb5* mouse lines model the microcephalic phenotypes observed in patients and that this phenotype can be attributed to mitotic defects in neuronal progenitors and massive p53-induced apoptosis. We further demonstrate that loss-of-function mutations in *Tubb5* are capable of causing microcephaly in the mouse; however, the E401K acts by a complex mechanism exhibiting subtle gain-of-function effects.

RESULTS

Tubb5 perturbation causes microcephaly in the mouse

In order to explore the genetic and cellular pathology underlying TUBB5 perturbations we engineered two conditional *Tubb5* transgenic mouse lines: a conditional knock-in of the E401K patient mutation and a conditional knockout (Fig. S1A). Both the conditional knock-in and the knockout lines rely on loxP sites flanking the terminal exon (exon 4). In the case of the E401K knock-in, a modified version of exon 4 containing the E401K amino acid substitution was inserted downstream of this exon, permitting its conditional activation. mRNA analysis showed that, in the absence of the Cre recombinase, the E401K mutation was not expressed (data not shown). We employed a nestin promoter to drive Cre recombinase (*Nestin-Cre*), allowing for the specific investigation of the E401K knock-in and the knockout in the developing brain (Tronche et al., 1999). In the presence of this Cre recombinase, cDNA sequencing confirmed that the E401K mutation is expressed, and qPCR analysis at embryonic day (E) 14.5 showed that *Tubb5* is expressed at similar levels as in controls (Fig. S1D).

We analysed adult mice, employing Nissl stains and volumetric magnetic resonance imaging (MRI). Unexpectedly, we found that heterozygous E401K animals expressing the Cre recombinase (*Tubb5*$^{E401K/+}$;*Nestin-Cre*) showed no significant reduction in brain size in comparison to littermate controls (*Tubb5*$^{E401K/+}$) (Fig. 1A,B,E,F). This contrasted with homozygous E401K animals

[1]Research Institute of Molecular Pathology (IMP), Vienna Biocenter (VBC), Dr. Bohr-Gasse 7, Vienna 1030, Austria. [2]Medical Scientist Training Program, Stony Brook University Medical Center, Stony Brook, NY 11794, USA. [3]Wellcome Trust Centre for Human Genetics, Roosevelt Drive, Oxford OX3 7BN, UK. [4]Institute for Molecular Biotechnology (IMBA), Vienna Biocenter (VBC), Dr. Bohr-Gasse 3, Vienna 1030, Austria.

*Author for correspondence (david.keays@imp.ac.at)

Received 7 October 2015; Accepted 15 February 2016

Development (2016) 143, 1126-1133 doi:10.1242/dev.131516

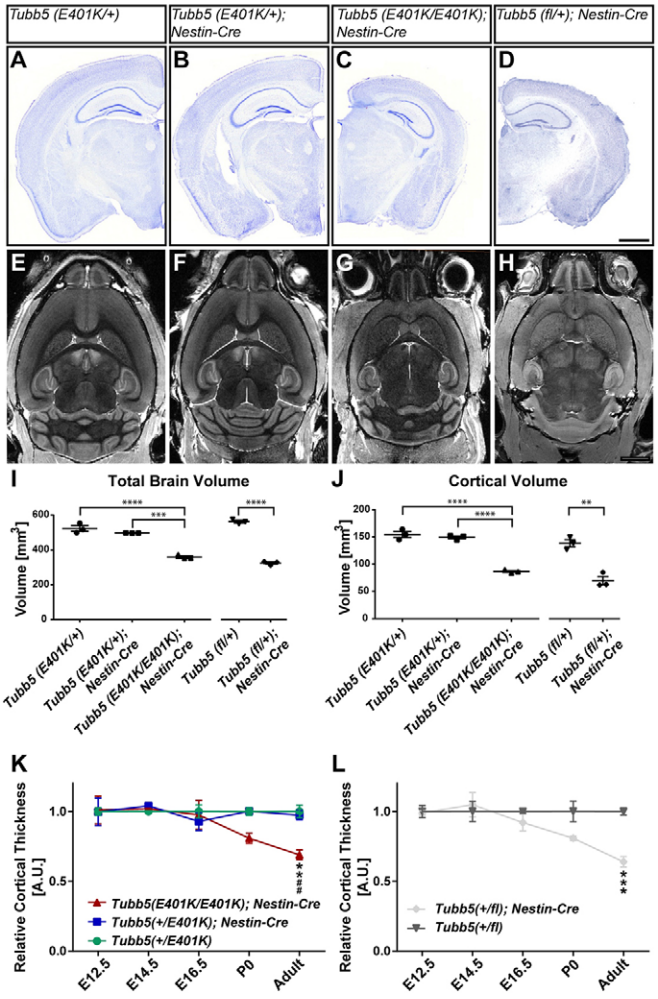

Fig. 1. Tubb5 perturbation causes microcephaly in the mouse. (A-D) Nissl-stained coronal sections of the adult brain of mice of the indicated genotypes. (E-H) Axial magnetic resonance images (MRIs) of adult mice brains of the indicated genotypes. (I,J) Quantification of total brain (I) and cortical (J) volume, including a heterozygous floxed line without Cre as an additional control. (K,L) Quantification of cortical thickness during development and in adulthood for the E401K knock-in (K) and the knockout (L) lines. (I-L) Mean±s.e.m. $^{*/\#}P<0.01$, $^{***}P<0.001$, $^{****}P<0.0001$ (* and # in K indicate significance relative to $Tubb5^{E401K/+}$ and $Tubb5^{E401K/+}$; *Nestin-Cre*, respectively) by (I,J) a one-way ANOVA with a Bonferroni post test for multiple comparisons for the knock-in and a two-tailed Student's *t*-test for the knockout and (K,L) a two-way ANOVA with a Bonferroni post test for multiple comparisons. $n=3$ for all conditions. Scale bars: 1 mm in D; 2 mm in H.

and heterozygous *Tubb5* null alleles, both of which presented with large reductions in total brain ($Tubb5^{E401K/E401K}$;*Nestin-Cre*, $P<0.0001$; $Tubb5^{fl/+}$;*Nestin-Cre*, $P<0.0001$; $n=3$) and cortical ($Tubb5^{E401K/E401K}$;*Nestin-Cre*, $P<0.0001$; $Tubb5^{fl/+}$;*Nestin-Cre*, $P=0.0025$; $n=3$) volume (Fig. 1C,D,G-J). This reduction was also observed in other brain regions, including the corpus callosum, cerebellum, hippocampus and putamen (Fig. S2D,E). Cortical thickness was similar in affected animals and wild-type littermate controls at E12.5, E14.5 and E16.5 (Fig. 1K,L). However, at postnatal day (P) 0 the cortex was notably thinner in affected lines, and severely reduced in adulthood ($Tubb5^{E401K/E401K}$;*Nestin-Cre*, $P<0.01$; $Tubb5^{fl/+}$;*Nestin-Cre*, $P<0.001$; $n=3$). This suggests that the underlying defect has its origin in development and is exacerbated postnatally (Fig. 1K,L). Attempts to generate adult homozygous null animals driven by *Nestin-Cre* were unsuccessful owing to prenatal and early postnatal lethality (no animals could be recovered past weaning age).

Taken together, these data show that our *Tubb5* mouse lines model the microcephaly described in humans with *TUBB5* mutations, and that loss-of-function mutations can result in phenotypes consistent with the tubulin-associated disease states.

Preservation of cortical architecture but loss of upper neuronal layers in *Tubb5* mutants

Next, we examined the cortical architecture of our *Tubb5* mutant lines, employing a number of laminar markers. Consistent with the human phenotype, we did not observe any gross defects in the laminar structure of the cortex when staining for Foxp2 (layer VI marker), Er81 (layer V marker; Etv1 – Mouse Genome Informatics) or Cux1 (layer II-IV marker) in the homozygous E401K animals or the heterozygous *Tubb5* null alleles (Fig. 2A-L, Fig. S3A-C). However, quantitation of these layers revealed a large reduction in the number of Cux1-positive superficial neurons in the *Nestin-Cre*-positive homozygous E401K animals and the heterozygous null animals ($Tubb5^{E401K/E401K}$;*Nestin-Cre*, $P<0.01$; $Tubb5^{fl/+}$;*Nestin-Cre*, $P=0.002$; $n=3$; Fig. 2O). As there was no difference in the number of Er81-positive and Foxp2-positive cells between affected animals and littermate controls, the relative contribution of layers II-IV to total cortical thickness was changed dramatically (Fig. 2M,N, Fig. S3D).

Neuronal progenitors in *Tubb5* mutant mice

As cortical lamination proceeds in an inside-out pattern, with the time of birth correlating with the cellular identity and final position of neurons (Greig et al., 2013), we explored the loss of upper-layer neurons by investigating the developing cortex at E14.5. We first asked whether the reduction in neuronal number might be attributed to a reduction in the number of neuronal progenitors (Fig. 3A-H, Fig. S4A,B).

Staining for Tbr2 (Eomes – Mouse Genome Informatics) revealed no significant difference in the number of intermediate progenitors in the *Nestin-Cre*-positive homozygous E401K animals or heterozygous null animals when compared with littermate controls at E14.5 (Fig. S4J). We did observe a small reduction in Sox2-positive apical progenitors in our heterozygous knockout animals that was not apparent in the homozygous E401K knock-in animals ($Tubb5^{fl/+}$;*Nestin-Cre*, $P=0.0494$; $Tubb5^{E401K/E401K}$;*Nestin-Cre*, $P>0.05$; $n=3$; Fig. 3A-D, Fig. S4A,I). Strikingly, in these knock-in animals we observed an increase in the number of ectopic Sox2-positive and Tbr2-positive progenitor cells that were not present in the heterozygous knockout (Sox2, $Tubb5^{E401K/E401K}$;*Nestin-Cre*, $P<0.01$; Tbr2, $Tubb5^{E401K/E401K}$;*Nestin-Cre*, $P<0.001$; $n=3$; Fig. 3C,G,M, Fig. S4D-F,K). Staining for the phosphorylated form of the intermediate filament component vimentin revealed that a subpopulation of these ectopic cells showed basal processes reminiscent of basal radial glial cells (Fig. S4G,H) (Florio and Huttner, 2014).

The presence of ectopic progenitors has been associated with defects in spindle orientation, which can lead to depletion of the progenitor pool and premature production of postmitotic neurons. This has been proposed to be the underlying cellular pathology responsible for microcephaly (Fish et al., 2006; Thornton and Woods, 2009). To assess spindle orientation in our mouse lines we stained for N-cadherin, γ-tubulin, phosphorylated histone H3 (pH3) and DNA at E14.5, permitting three-dimensional assessment of the spindle angles relative to the ventricular surface (Xie et al., 2013) (Fig. 3P). Comparison of spindle orientation in the heterozygous knockout animals with littermate control animals revealed that the

Development (2016) 143, 1126-1133 doi:10.1242/dev.131516

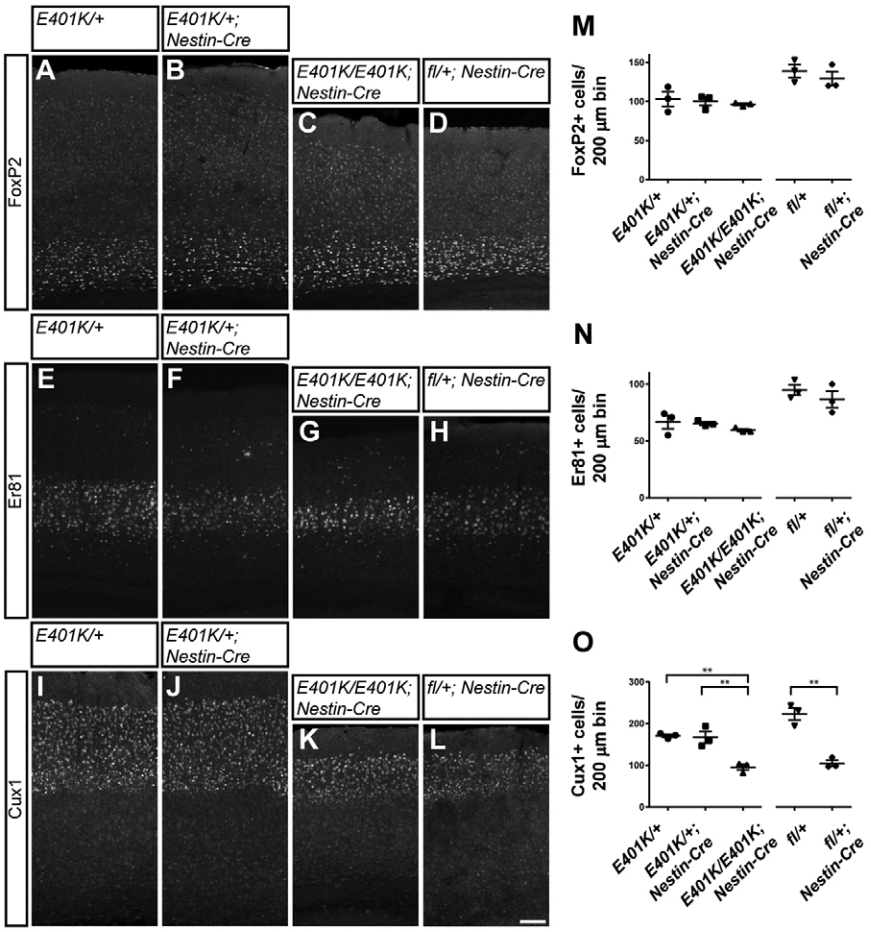

Fig. 2. *Tubb5*-mediated microcephaly is caused by a specific loss of upper-layer neurons. (A-L) Immunostainings for cortical layers of adult brains of mice of the indicated *Tubb5* genotypes. Shown are the layer VI marker Foxp2 (A-D), the layer V marker Er81 (E-H) and the layer II-IV marker Cux1 (I-L). (M-O) Quantification of the number of cells positive for Foxp2 (M), Er81 (N) and Cux1 (O) in a cortical area of 200 µm width. The laminar structure of the cortex is preserved in all genotypes; however, there is a large reduction in the number of superficial Cux1-positive neurons in homozygous E401K mutants and heterozygous knockout animals. Error bars show mean±s.e.m. $^{**}P<0.01$ by a one-way ANOVA with a Bonferroni post test for multiple comparisons for the knock-in and a two-tailed Student's *t*-test for the knockout. $n=3$ for all conditions. Scale bar: 100 µm.

vast majority of divisions were in the horizontal plane. In the case of E401K homozygous animals a significantly higher percentage of vertical orientations were observed compared with controls (*Tubb5*$^{E401K/E401K}$*;Nestin-Cre*, $P<0.01$, $n=4$ animals, $n>76$ cells; Fig. 3Q, Fig. S5A-F).

We conclude that the presence of ectopic progenitors in the E401K mutant mice might result from changes in spindle orientation, but this does not have a significant impact on the number of progenitors and is unlikely to account for the severe microcephalic phenotype observed in adulthood.

Distinct mitotic defects cause p53-mediated apoptosis in the knock-in and the knockout

Next, we examined our mutant lines for defects in mitosis by staining for the M-phase marker pH3 at E14.5. A comparison with littermate controls revealed no significant difference in heterozygous knockout animals, but a notable increase in the number of pH3-positive cells in the E401K homozygous mutants (*Tubb5*$^{E401K/E401K}$*;Nestin-Cre*, $P<0.05$; *Tubb5*$^{fl/+}$*;Nestin-Cre*, $P>0.05$; $n=3$; Fig. 3I-L,N,O). One explanation for this increase is a lengthening of M phase, caused by a delay in mitotic progression. To assess this we stained for the chromosomal passenger complex aurora kinase B, pH3 and with Hoechst, permitting identification and scoring of cells in metaphase and anaphase/telophase (Fig. 4A-F, Fig. S6A,B) (Adams et al., 2001). We observed an enrichment of cells in metaphase in the homozygous E401K mutant animals in comparison to littermate controls (Fig. 4O). These data are consistent with the observed increase in pH3 staining, and suggest stalling of the cell cycle during M phase. This phenotype was absent from our heterozygous knockout animals; however, in these animals we observed a significant increase in ectopic DNA elements, such as chromosome bridges or globular Hoechst-positive structures outside the metaphase plate (Fig. 4G-N,P).

As defects in mitotic progression and lagging chromosomes have been associated with apoptosis in the embryonic brain, we stained for cleaved caspase 3 in our mutant lines (Insolera et al., 2014; Marthiens et al., 2013) (Fig. 4Q-T, Fig. S6C). We observed a significant induction of apoptosis in both the mutant lines (*Tubb5*$^{E401K/E401K}$*;Nestin-Cre*, $P<0.05$; *Tubb5*$^{fl/+}$*;Nestin-Cre*, $P=0.0067$; $n=3$; Fig. 4Y). Consistent with previous reports we also observed a concomitant increase of the upstream regulator p53 (Trp53 – Mouse Genome Informatics) (*Tubb5*$^{E401K/E401K}$*;Nestin-Cre*, $P<0.0001$; *Tubb5*$^{fl/+}$*;Nestin-Cre*, $P<0.0001$; $n=3$; Fig. 4U-X, Z, Fig. S6D) (Insolera et al., 2014; Marthiens et al., 2013). To confirm the role of p53 as an apoptotic driver we crossed the heterozygous *Tubb5* knockout animals (*Tubb5*$^{fl/+}$*;Nestin-Cre*) onto a *p53* null background (Marino et al., 2000). This resulted in a complete rescue of the prolific apoptosis in the heterozygous knockout animals ($P<0.05$; $n=2$; Fig. S6E-G). We conclude that distinct defects during mitosis drive p53-dependent apoptosis in our *Tubb5* mutant mouse lines, leading to a smaller brain size.

Defects in mitotic progression are dependent on the dose of Tubb5

Finally, we investigated the origin of the different phenotypes in our *Tubb5* mutant lines. Specifically, we sought to establish whether the mitotic progression defect and ectopic progenitors observed in

Development (2016) 143, 1126-1133 doi:10.1242/dev.131516

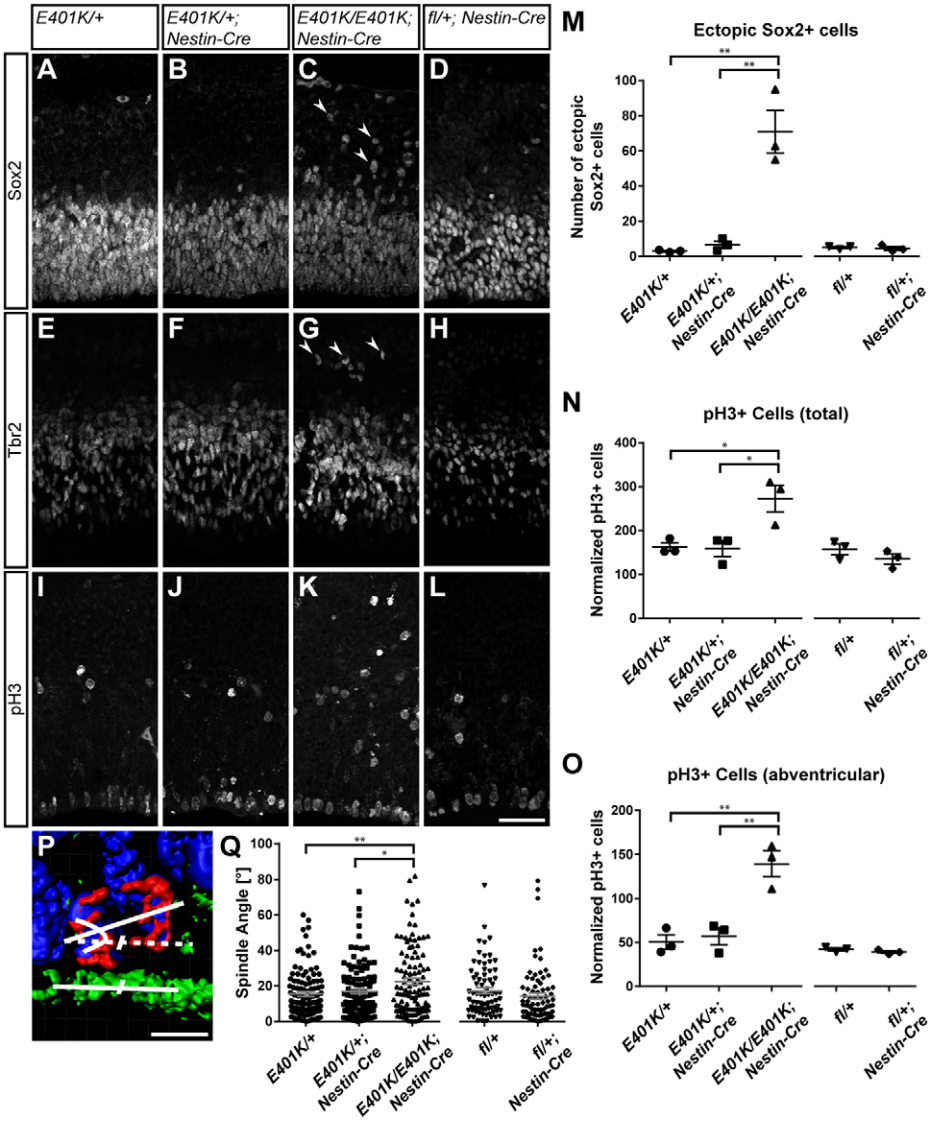

Fig. 3. Ectopic progenitors and an increased mitotic index in the homozygous E401K mutant mouse. (A-L) Immunostainings of the embryonic cortex (E14.5) for (A-D) Sox2-positive radial glial cells, (E-H) Tbr2-positive intermediate progenitors and (I-L) pH3-positive mitotic cells for mice of the indicated *Tubb5* genotypes. Arrowheads (C,G) indicate ectopic cells positive for the respective markers. (M-O) Quantification of the number of ectopic Sox2-positive cells (M), the number of pH3-positive cells (N) and the number of abventricular pH3-positive cells (O) for each genotype. The number of pH3-positive cells was normalised to the length of the ventricular surface. (P) Representative 3D reconstruction of a mitotic cell stained for pH3 (red), γ-tubulin (green), N-cadherin (green) and DNA (Hoechst, blue). Measurement of the spindle orientation employed a line drawn between the centrosomes marked by γ-tubulin and a plane defined by five points on the N-cadherin-marked surface (represented by the parallel solid and dashed lines). (Q) Quantification of spindle angle measurements for all five genotypes. Note the significant increase of the mean spindle angle in the homozygous knock-in. (M-O,Q) Error bars show the mean±s.e.m. **P*<0.05, ***P*<0.01 by one-way ANOVA with a Bonferroni post test for multiple comparisons for the knock-in and a two-tailed Student's *t*-test for the knockout. *n*=3 for all conditions except Q (*n*=4 animals, *n*≥76 mitotic cells per condition). Scale bars: 50 µm in L; 5 µm in P.

homozygous E401K mutant animals, but absent from the heterozygous knockout animals, could be attributed to the dosage of functional Tubb5. We therefore examined the cortices of homozygous knockout animals, which did not survive into adulthood but are viable at E14.5. Aurora B, pH3 and Hoechst staining revealed a severe mitotic progression defect and abnormal chromosomal elements (Fig. 5A-H). This was accompanied by a massive increase in the number of cells positive for cleaved caspase 3 (P=0.0004; n=3) and p53 (P=0.003; n=3) (Fig. 5I-N). Interestingly, the orientation of the spindle in mitotic progenitors in homozygous knockout animals was indistinguishable from that of controls (Fig. S7D-G), and Sox2 staining revealed no increase in ectopic progenitors (P>0.05; n=3; Fig. S7A-C).

These data show that Tubb5 has a dose-dependent effect on cell cycle progression and apoptosis. However, the presence of ectopic progenitors in the homozygous E401K mouse indicates that this missense mutation has a more complex mode of action, with subtle gain-of-function effects.

DISCUSSION

In this study we have explored the genetic and cellular mechanisms that cause TUBB5-associated microcephaly by exploiting two new mouse models: a conditional E401K knock-in, and a conditional knockout animal. Both lines present with severe microcephaly, recapitulating the primary pathological feature observed in affected patients. Comparison of these lines with each other and littermate controls revealed that the reduction in brain size is due to distinct mitotic defects in apical progenitors, which drive p53-associated apoptosis. Our results demonstrate that the severity of phenotypes represent a continuous spectrum that is dependent on the dosage of functional Tubb5 (Fig. 6).

This work and a number of recent studies have contributed to a growing understanding of the cellular aetiology that is responsible for microcephaly. Those genes that are known to cause this disease, which include *ASPM*, *CDK5RAP2*, *WDR62*, *MCPH1*, *CEP152* and *STIL*, are intimately associated with the mitotic apparatus and centrosomes (Alcantara and O'Driscoll, 2014). Although mouse models for these genes have not always resulted in strong phenotypes, some have revealed defects in asymmetric cell division (Fish et al., 2006; Gruber et al., 2011; Pulvers et al., 2010). These defects, which prematurely shift the output of progenitors to neurons, have been proposed to provide a common functional link between the different microcephaly-causing genes (Thornton and Woods, 2009; Woods et al., 2005). This model, however, has increasingly been challenged.

Development (2016) 143, 1126-1133 doi:10.1242/dev.131516

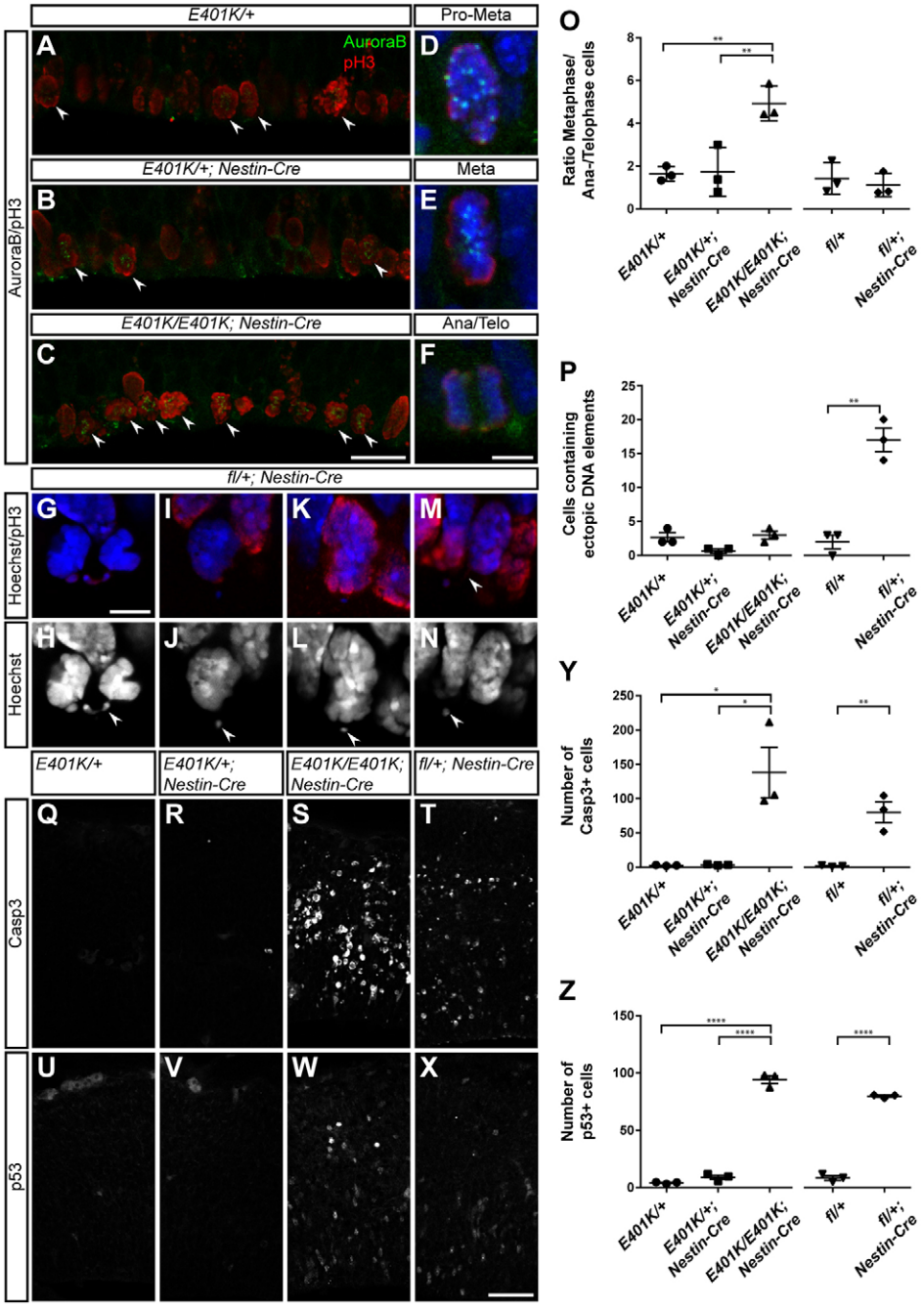

Fig. 4. Defects in mitotic progression and p53-associated massive apoptosis in *Tubb5* mutant mice. (A-C) Immunostainings for aurora B and pH3 for mice of the indicated *Tubb5* genotypes. Arrowheads indicate cells that were scored to be in metaphase. (D-F) Representative images for cells in pro-metaphase, metaphase and anaphase/telophase. (G-N) Immunostainings for pH3 and Hoechst nuclear staining for the heterozygous knockout line. (H,J,L,N) Greyscale images of the Hoechst staining above, with arrowheads indicating ectopic DNA elements – a mitotic chromosome bridge in the case of H. The arrowhead in M indicates a pH3-positive bridge connecting the ectopic DNA element to the nucleus. (O) Quantification of the ratio of metaphase and anaphase/telophase cells for all genotypes for all mitotic cells in the cortex. (P) Quantification of the appearance of ectopic DNA elements at the ventricular surface. (Q-X) Immunostainings of the embryonic cortex (E14.5) for the apoptotic marker cleaved caspase 3 (Q-T) and the apoptosis regulator p53 (U-X). (Y,Z) Quantification of the number of cleaved caspase 3-positive cells (Y) and the number of p53-positive cells (Z) per cortical image. Both the homozygous knock-in and the heterozygous knockout show a significant increase in the number of cells positive for cleaved caspase 3 and p53. (O,P,Y,Z) Error bars show the mean±s.e.m. **P*<0.05, ***P*<0.01, *****P*<0.0001 by one-way ANOVA with a Bonferroni post test for multiple comparisons for the knock-in and a two-tailed Student's *t*-test for the knockout. *n*=3 for all conditions. Scale bars: 20 µm in C; 5 µm in F,G; 50 µm in X.

Niswander and colleagues have recently shown that a mouse model of *Wdr62* does not present with abnormal spindle orientation, but rather that defects in spindle stability promote mitotic arrest and, consequently, cell death (Chen et al., 2014). Our conditional knockout mouse likewise presents with normal spindle orientation, but severe microcephaly due to massive apoptosis associated with p53 upregulation. The involvement of p53 in the pathogenesis of microcephaly has been further highlighted by recent studies that employed mouse models to alter the number of centrioles in radial glial progenitors (Insolera et al., 2014; Marthiens et al., 2013). These studies, along with ours, suggest that microcephaly is caused by a variety of defects during mitosis, including temporal perturbation of the cell cycle, impaired spindle stability, multi-polar spindles, and aneuploidy, which then engage apoptotic mechanisms through p53 induction.

Here, we report the specific loss of upper-layer neurons in our mouse models, whereas those in the deeper layers are largely preserved. This could reflect the onset of *Nestin-Cre*-induced recombination and the half-life of the Tubb5 protein. This Cre line reaches its peak of recombination at E10.5-E11.5, showing efficient recombination by E12.5 (Dubois et al., 2006; Insolera et al., 2014). However, the stability of existing Tubb5 transcript and protein might prevent any defects prior to E14.5, when deep-layer neurons are generated (Greig et al., 2013). Alternatively, the preservation of deep-layer neurons might reflect functional complementation by another beta-tubulin isoform. The tubulin gene family contains multiple isoforms, with dynamic expression patterns (Breuss et al., 2015). It is conceivable that one of these isoforms (e.g. Tubb2b) is able to compensate for the lack of Tubb5 at earlier time points, but not at later stages. Finally, it is possible that progenitor cells exhibit distinct sensitivities to spindle

Development (2016) 143, 1126-1133 doi:10.1242/dev.131516

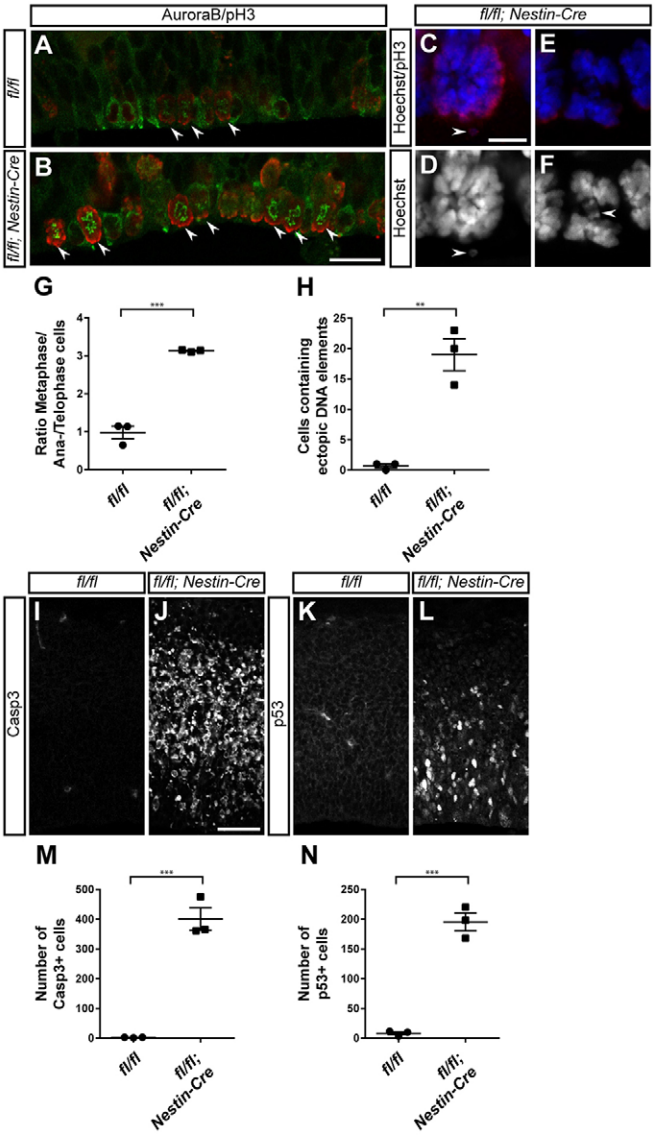

Fig. 5. Homozygous knockout of *Tubb5* induces mitotic progression defects, ectopic DNA elements and enhances apoptosis. (A,B) Immunostainings for aurora B and pH3 for the *Tubb5*$^{fl/fl}$*; Nestin-Cre* homozygous knockout and a *Tubb5*$^{fl/fl}$ littermate control. Arrowheads indicate cells scored to be in metaphase. (C-F) Immunostaining for pH3 and Hoechst nuclear staining for the homozygous knockout line. (D,F) Greyscale images of the Hoechst staining above, with arrowheads indicating ectopic DNA elements – a mitotic chromosome bridge in the case of F. Arrowhead in C indicates pH3 signal on an ectopic DNA element. (G,H) Quantification of the ratio of metaphase and anaphase/telophase cells (G) and the appearance of ectopic DNA elements at the ventricular surface (H) for the homozygous knockout line. (I-L) Immunostainings for the apoptotic marker cleaved caspase 3 (I,J) and the apoptosis regulator p53 (K,L) for the *Tubb5* homozygous knockout and littermate controls. (M,N) Quantification of the number of cleaved caspase 3-positive cells (M) and the number of p53-positive cells (N) per cortical image. The homozygous knockout shows a significant increase in the number of cells positive for caspase 3 and p53. (G,H,M,N) Error bars show the mean±s.e.m. ***P*<0.01, ****P*<0.001 by two-tailed Student's *t*-test. *n*=3 for all conditions. Scale bars: 20 µm in B; 5 µm in C; 50 µm in J.

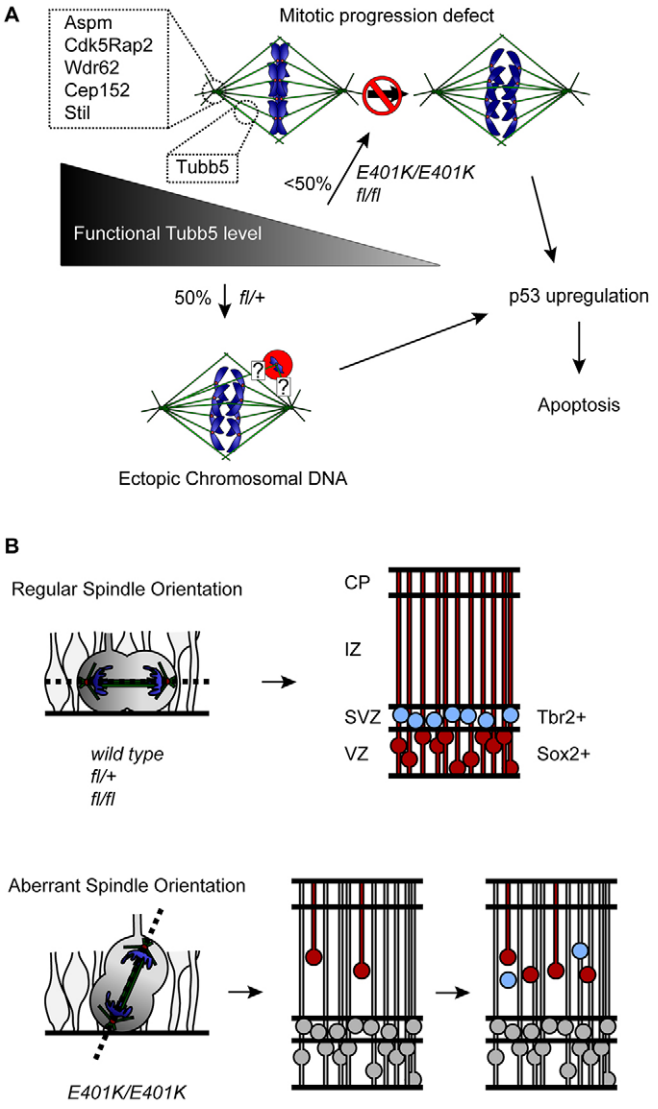

Fig. 6. Model for the effect of Tubb5 perturbation in murine cortical progenitors. (A) Upon depletion of functional Tubb5 by 50%, ectopic DNA elements appear that are not sufficient to arrest the cell cycle but nonetheless activate the p53 pathway and induce apoptosis. If functional levels of Tubb5 are below 50% this results in an outright mitotic progression defect, upregulation of p53 and apoptosis. Also depicted are some of the known microcephaly genes associated with the centrosome (*Aspm*, *Cdk5rap2*, *Wdr62*, *Cep152* and *Stil*). (B) Our data suggest that the E401K mutation also has a gain-of-function or neomorphic effect on the mitotic spindle. Whereas heterozygous and homozygous *Tubb5* knockout animals exhibit no defects in spindle orientation, in our homozygous E401K animals we observed a higher percentage of vertical orientations in comparison to control mice. We hypothesise that this defect is responsible for the increase in ectopic progenitors that we observe in this mouse line. CP, cortical plate; IZ, intermediate zone; SVZ, subventricular zone; VZ, ventricular zone.

perturbations during neuronal development. A specific loss of upper-layer neurons following depletion of Nde1 in a full-body homozygous knockout supports this idea (Feng and Walsh, 2004).

This study has also provided insight into the genetic mechanisms by which tubulin mutations cause human disease. It is known that some tubulin mutations, including E401K, cause defects in the chaperone-mediated folding pathway, impairing tubulin heterodimer formation. These data alone would suggest that the mutations act by loss of function, but the absence of disease-causing null alleles has lent weight to the argument that all tubulin mutations act by gain of function (Hu et al., 2014; Kumar et al., 2010). This contention has been further supported by overexpression of these folding mutations *in vivo* by *in utero* electroporation, which resulted in severe phenotypes (Breuss et al., 2012; Ngo et al., 2014). Characterisation of our *Tubb5* conditional

Development (2016) 143, 1126-1133 doi:10.1242/dev.131516

knockout mouse demonstrated that null alleles can result in severe phenotypes consistent with the tubulinopathies. However, detailed analysis of the E401K mutant mouse has shown that the mode of action in the case of this missense mutation is complex. Although we cannot exclude the possibility that the ectopic Sox2-positive progenitors in the E401K mouse line are a consequence of dose dependency, their absence in the knockout line suggests that this missense mutation has a subtle hypermorphic or neomorphic effect. This, however, does not seem to be the mechanism that drives microcephaly, which we attribute to apoptosis resulting from mitotic defects associated with a reduction in the pool of functional heterodimers.

Finally, our data highlight the limitation of studying tubulin mutations by overexpressing disease-causing mutations in cell culture and *in vivo* by electroporation. FLAG-tagged variants of Tubb5 with the E401K mutation completely fail to incorporate into the microtubule cytoskeleton in Neuro2A cells (Breuss et al., 2012), but some mutant heterodimers must fold correctly and incorporate *in vivo* in our E401K mouse. Similarly, overexpression of the E401K mutation by *in utero* electroporation revealed no induction of apoptosis (Breuss et al., 2012), whereas our present data show that cell death underpins the microcephalic phenotype in our mouse lines. It is therefore evident that if we are to understand the pathology that underlies the expanding spectrum of tubulin-associated disease states then *in vivo* mouse models will be vital.

MATERIALS AND METHODS

Generation and maintenance of transgenic mouse lines

Targeting constructs were generated by modifying a BAC containing the *Tubb5* gene (*RP24-330C1*) with the Red/ET system (Gene Bridges). These were linearised and electroporated into A9 embryonic stem cells (ESCs) derived from 129/Ola and C57BL/6J hybrids (Neely et al., 2010). ESC clones resistant to G418 (geneticin) were picked and grown and then DNA was extracted by isopropanol precipitation. For Southern blot analysis DNA was digested with *Eco*RI (Roche, 10200310001), run on a 0.7% agarose gel (in TAE), denatured (10 M NaOH, 1.5 M NaCl), neutralised (0.05 M Na_3PO_4, pH 7.2), transferred to a Porablot NY Plus membrane with 20× SSC overnight (Porablot, 741240) and cross-linked the next day. The hybridisation probe (365 bp PCR product of primers Tubb5_SB_F and Tubb5_SB_R; Table S1) was radioactively labelled and purified according to the manufacturer's protocols (Rediprime II DNA Labelling System, GE Healthcare, RPN1633; Illustra ProbeQuant G-50 Micro Columns, GE Healthcare, 28-9034-08) before incubation with hybridisation solution (Sigma, H7033) overnight at 65°C in a rolling shaker, followed by washing and development.

Successful recombination of the upstream loxP site was confirmed by PCR analysis (primers Tubb5_LoxP_F and Tubb5_LoxP_R). Positive ESC clones were injected into C57BL/6J blastocysts to generate chimeras (Gossler et al., 1986). Mice were maintained at the animal facilities at the Institute of Molecular Pathology (IMP), Vienna, under specific pathogen-free (SPF) conditions on a 14:10 h light:dark cycle. Mice were genotyped for the presence of the transgene by PCR analysis of genomic DNA extracted from ear clips. Mice were kept in a mixed background and all experiments presented use littermate controls. Prior to experiments, mice were crossed to a mouse line expressing the Flp recombinase under the control of a beta-actin promoter to remove the neomycin resistance cassette [in-house bred derivative of the B6.Cg-Tg(ACTFLPe)9205Dym/J line, Jackson Labs]. The *p53* conditional knockout mice used in this study were modified such that exons 2-10 were flanked by loxP sites. These mice were obtained from the Jackson Labs ($Trp53^{tm1Brn}$) and maintained on a C57BL/6J background.

qPCR was performed as previously described (Braun et al., 2010; Breuss et al., 2012). Primers are listed in Table S1. All procedures were carried out according to legal requirements and covered by an approved license (M58/006093/2011/14) from the city of Vienna, Austria.

Nissl staining and immunohistochemistry

Embryos were harvested at E14.5 and E16.5, postfixed in 4% paraformaldehyde (PFA) overnight, dehydrated in 30% sucrose, embedded in Neg-50 Frozen Section Medium (Richard-Allan Scientific, 6502-APD) and sectioned on a cryostat (12 µm). Brains of adult animals (12-16 weeks of age) were dissected following perfusion with 0.9% NaCl followed by 4% PFA. Sections for Nissl staining were dried, washed in PBS and incubated in Cresyl Violet for 3 min [0.25% Cresyl Violet acetate (Sigma, C5042) in distilled water with ten drops of glacial acetic acid added per 100 ml of solution]. After a short wash in distilled water, sections were dehydrated in an alcohol series (30%, 70%, 96% and 100% ethanol, 2 min each) and xylol (twice, 2 min each), and left until mounting with DPX mountant (Fluka, 44581). Images were acquired on a Mirax slide scanner (Zeiss).

For immunohistochemistry, sections were incubated with the primary antibody overnight in blocking solution supplemented with Triton X-100 and donkey serum or BSA (see Table S2). For all stainings, antigen retrieval was performed with Antigen Unmasking Solution (Vector Laboratories, H-3301). Slides were heated from room temperature to 90°C in a water bath and then placed at room temperature for 30 min prior to incubation with the primary antibody overnight (14-16 h) at 4°C. The next day, sections were washed three times in PBS (5 min each) before application of a species-specific secondary antibody (Molecular Probes, A-10037, A-11057, A-10042, A-21206; 1:500) for 1 h in blocking solution at 4°C. Following staining for 5 min with Hoechst 33342 fluorescent stain in PBS (1:2000), slides were mounted with Fluorescent Mounting Medium (Dako, S302380).

Magnetic resonance imaging and area segmentation

For MRI analysis, adult mice were perfused with 0.9% NaCl and 4% PFA supplemented with 10% ProHance Solution (Bracco Imaging Group, 4002750). MR images were acquired with a 15.2 T Biospec horizontal bore scanner (Bruker BioSpin) and BFG6S-100 actively shielded gradient system (750 mT/m maximum gradient strength). A quadrature transmit/receive volume coil (23 mm inner diameter; Bruker BioSpin) was used. A T1-weighted multi-slice multi-echo (MSME) 3D sequence was used with TR/TE 20/3.7 ms, 1.8×1.6×1.6 cm^3 field of view, 50×50×100 μm^3 spatial resolution, four averages. Total imaging time was 1 h 21 min. Each 3D image set was manually segmented using Amira 5.6 (Visualization Science Group). The delineation of different brain structures was performed in the axial plane and subsequently controlled in the other two planes. A mouse brain atlas was used as a reference (Paxinos and Franklin, 2004). The brain surface and structures were delineated based on the MRI signal intensity differences. The Amira software package was used for volume calculation of different brain regions and a two-way ANOVA with a Bonferroni correction for multiple comparisons was employed to test significance.

Quantifications

To determine cortical thickness during development, Nissl sections (E12.5, E14.5, E16.5, P0) were scanned and matched cortical regions of all genotypes were measured. For Sox2, Tbr2, pH3, p53 and cleaved caspase 3 quantifications, images were captured with an LSM710 (Zeiss) and the number of positive cells in the cortex in a field of view measuring 340×340 µm were counted. For each animal, four images were quantitated and an average was obtained. In the case of pH3-positive cells this count was normalised to the length of the ventricle.

For the quantification of mitotic progression and the occurrence of ectopic DNA elements, images were captured with an LSM710 and cells were counted in a field of view measuring 236×236 µm covering the thickness of the entire section in *z*. Spindle orientation measurements were performed as described previously (Juschke et al., 2014; Postiglione et al., 2011; Xie et al., 2013). All cells assessed for our spindle orientation experiments were directly adjacent to the ventricular surface.

For adult layer marker quantifications (Foxp2, Cux1, Er81), confocal images of coronal sections were acquired on an LSM710 and a 200 µm-wide box was positioned across the cortex. For each animal, positive cells were counted on four images and the number averaged. To determine the relative thickness, layers were measured on the same sections. All cell counting was performed blind to genotype. Statistical significance was determined by

Development (2016) 143, 1126-1133 doi:10.1242/dev.131516

application of a two-tailed Student's *t*-test or a one-way ANOVA with a Bonferroni post test for multiple comparisons with GraphPad Prism. For cortical thickness during development and the relative layer thickness a two-way ANOVA with a Bonferroni post test for multiple comparisons was employed.

Acknowledgements

We acknowledge the IMP-IMBA bio-optical facilities, the transgenic services and the animal attendants for assistance. MRI acquisition was performed by the Preclinical Imaging Facility of the Campus Science Support Facilities (CSF). We extend our gratitude to the Jürgen Knoblich and Jan-Michael Peters laboratories for help with reagents and protocols. Thanks are also due to Simon Hippenmeyer and Fiona Francis for reading and commenting on the manuscript.

Competing interests

The authors declare no competing or financial interests.

Author contributions

Mice were generated by M.B., U.E., D.A.K., F.W.V. and B.W. Experiments were performed by M.B. with help from T.F., K.C., T.G., L.U. and N.Y. Data analysis was performed by M.B. The project was designed by M.B. and D.A.K. The manuscript was prepared by M.B. and D.A.K.

Funding

We are indebted to Boehringer Ingelheim and the Austrian Science Fund (FWF) for funding this research [I914, P21092].

Supplementary information

Supplementary information available online at
http://dev.biologists.org/lookup/suppl/doi:10.1242/dev.131516/-/DC1

References

Adams, R. R., Carmena, M. and Earnshaw, W. C. (2001). Chromosomal passengers and the (aurora) ABCs of mitosis. *Trends Cell Biol.* **11**, 49-54.

Alcantara, D. and O'Driscoll, M. (2014). Congenital microcephaly. *Am. J. Med. Genet. C Semin. Med. Genet.* **166**, 124-139.

Ayala, R., Shu, T. and Tsai, L.-H. (2007). Trekking across the brain: the journey of neuronal migration. *Cell* **128**, 29-43.

Bahi-Buisson, N., Poirier, K., Fourniol, F., Saillour, Y., Valence, S., Lebrun, N., Hully, M., Bianco, C. F., Boddaert, N., Elie, C. et al. (2014). The wide spectrum of tubulinopathies: what are the key features for the diagnosis? *Brain* **137**, 1676-1700.

Braun, A., Breuss, M., Salzer, M. C., Flint, J., Cowan, N. J. and Keays, D. A. (2010). Tuba8 is expressed at low levels in the developing mouse and human brain. *Am. J. Hum. Genet.* **86**, 819-822; author reply 822-813.

Breuss, M. and Keays, D. A. (2014). Microtubules and neurodevelopmental disease: the movers and the makers. In *Cellular and Molecular Control of Neuronal Migration* (ed. L. Nguyen and S. Hippenmeyer), pp. 75-96. Dordrecht: Springer.

Breuss, M., Heng, J. I, Poirier, K., Tian, G., Jaglin, X. H., Qu, Z., Braun, A., Gstrein, T., Ngo, L., Haas, M. et al. (2012). Mutations in the β-tubulin gene TUBB5 cause microcephaly with structural brain abnormalities. *Cell Rep.* **2**, 1554-1562.

Breuss, M., Morandell, J., Nimpf, S., Gstrein, T., Lauwers, M., Hochstoeger, T., Braun, A., Chan, K., Sanchez Guajardo, E. R., Zhang, L. et al. (2015). The expression of Tubb2b undergoes a developmental transition in murine cortical neurons. *J. Comp. Neurol.* **523**, 2161-2186.

Chen, J.-F., Zhang, Y., Wilde, J., Hansen, K. C., Lai, F. and Niswander, L. (2014). Microcephaly disease gene Wdr62 regulates mitotic progression of embryonic neural stem cells and brain size. *Nat. Commun.* **5**, 3885.

Dent, E. W., Gupton, S. L. and Gertler, F. B. (2011). The growth cone cytoskeleton in axon outgrowth and guidance. *Cold Spring Harb. Perspect. Biol.* **3**, a001800.

Dickson, B. J. (2002). Molecular mechanisms of axon guidance. *Science* **298**, 1959-1964.

Dubois, N. C., Hofmann, D., Kaloulis, K., Bishop, J. M. and Trumpp, A. (2006). Nestin-Cre transgenic mouse line Nes-Cre1 mediates highly efficient Cre/loxP mediated recombination in the nervous system, kidney, and somite-derived tissues. *Genesis* **44**, 355-360.

Feng, Y. and Walsh, C. A. (2004). Mitotic spindle regulation by Nde1 controls cerebral cortical size. *Neuron* **44**, 279-293.

Fish, J. L., Kosodo, Y., Enard, W., Paabo, S. and Huttner, W. B. (2006). Aspm specifically maintains symmetric proliferative divisions of neuroepithelial cells. *Proc. Natl. Acad. Sci. USA* **103**, 10438-10443.

Florio, M. and Huttner, W. B. (2014). Neural progenitors, neurogenesis and the evolution of the neocortex. *Development* **141**, 2182-2194.

Gossler, A., Doetschman, T., Korn, R., Serfling, E. and Kemler, R. (1986). Transgenesis by means of blastocyst-derived embryonic stem cell lines. *Proc. Natl. Acad. Sci. USA* **83**, 9065-9069.

Greig, L. C., Woodworth, M. B., Galazo, M. J., Padmanabhan, H. and Macklis, J. D. (2013). Molecular logic of neocortical projection neuron specification, development and diversity. *Nat. Rev. Neurosci.* **14**, 755-769.

Gruber, R., Zhou, Z., Sukchev, M., Joerss, T., Frappart, P.-O. and Wang, Z.-Q. (2011). MCPH1 regulates the neuroprogenitor division mode by coupling the centrosomal cycle with mitotic entry through the Chk1-Cdc25 pathway. *Nat. Cell Biol.* **13**, 1325-1334.

Hu, W. F., Chahrour, M. H. and Walsh, C. A. (2014). The diverse genetic landscape of neurodevelopmental disorders. *Annu. Rev. Genomics Hum. Genet.* **15**, 195-213.

Insolera, R., Bazzi, H., Shao, W., Anderson, K. V. and Shi, S.-H. (2014). Cortical neurogenesis in the absence of centrioles. *Nat. Neurosci.* **17**, 1528-1535.

Jaglin, X. H., Chelly, J. and Bahi-Buisson, N. (2012). Tubulin-related malformations of cortical development. In *Cytoskeleton and Human Disease* (ed. M. Kavallaris) , pp. 315-341. New York: Humana.

Juschke, C., Xie, Y., Postiglione, M. P. and Knoblich, J. A. (2014). Analysis and modeling of mitotic spindle orientations in three dimensions. *Proc. Natl. Acad. Sci. USA* **111**, 1014-1019.

Kuijpers, M. and Hoogenraad, C. C. (2011). Centrosomes, microtubules and neuronal development. *Mol. Cell. Neurosci.* **48**, 349-358.

Kumar, R. A., Pilz, D. T., Babatz, T. D., Cushion, T. D., Harvey, K., Topf, M., Yates, L., Robb, S., Uyanik, G., Mancini, G. M. S. et al. (2010). TUBA1A mutations cause wide spectrum lissencephaly (smooth brain) and suggest that multiple neuronal migration pathways converge on alpha tubulins. *Hum. Mol. Genet.* **19**, 2817-2827.

Marino, S., Vooijs, M., van Der Gulden, H., Jonkers, J. and Berns, A. (2000). Induction of medulloblastomas in p53-null mutant mice by somatic inactivation of Rb in the external granular layer cells of the cerebellum. *Genes Dev.* **14**, 994-1004.

Marthiens, V., Rujano, M. A., Pennetier, C., Tessier, S., Paul-Gilloteaux, P. and Basto, R. (2013). Centrosome amplification causes microcephaly. *Nat. Cell Biol.* **15**, 731-740.

Neely, G. G., Kuba, K., Cammarato, A., Isobe, K., Amann, S., Zhang, L., Murata, M., Elmén, L., Gupta, V., Arora, S. et al. (2010). A global in vivo Drosophila RNAi screen identifies NOT3 as a conserved regulator of heart function. *Cell* **141**, 142-153.

Ngo, L., Haas, M., Qu, Z., Li, S. S., Zenker, J., Teng, K. S. L., Gunnersen, J. M., Breuss, M., Habgood, M., Keays, D. et al. (2014). TUBB5 and its disease-associated mutations influence the terminal differentiation and dendritic spine densities of cerebral cortical neurons. *Hum. Mol. Genet.* **23**, 5147-5158.

Paxinos, G. and Franklin, K. B. (2004). *The Mouse Brain in Stereotaxic Coordinates*. Houston: Gulf Professional Publishing.

Postiglione, M. P., Jüschke, C., Xie, Y., Haas, G. A., Charalambous, C. and Knoblich, J. A. (2011). Mouse inscuteable induces apical-basal spindle orientation to facilitate intermediate progenitor generation in the developing neocortex. *Neuron* **72**, 269-284.

Pulvers, J. N., Bryk, J., Fish, J. L., Wilsch-Brauninger, M., Arai, Y., Schreier, D., Naumann, R., Helppi, J., Habermann, B., Vogt, J. et al. (2010). Mutations in mouse Aspm (abnormal spindle-like microcephaly associated) cause not only microcephaly but also major defects in the germline. *Proc. Natl. Acad. Sci. USA* **107**, 16595-16600.

Smith, B. N., Ticozzi, N., Fallini, C., Gkazi, A. S., Topp, S., Kenna, K. P., Scotter, E. L., Kost, J., Keagle, P., Miller, J. W. et al. (2014). Exome-wide rare variant analysis identifies TUBA4A mutations associated with familial ALS. *Neuron* **84**, 324-331.

Thornton, G. K. and Woods, C. G. (2009). Primary microcephaly: do all roads lead to Rome? *Trends Genet.* **25**, 501-510.

Tischfield, M. A., Cederquist, G. Y., Gupta, M. L. and Engle, E. C. (2011). Phenotypic spectrum of the tubulin-related disorders and functional implications of disease-causing mutations. *Curr. Opin. Genet. Dev.* **21**, 286-294.

Tronche, F., Kellendonk, C., Kretz, O., Gass, P., Anlag, K., Orban, P. C., Bock, R., Klein, R. and Schütz, G. (1999). Disruption of the glucocorticoid receptor gene in the nervous system results in reduced anxiety. *Nat. Genet.* **23**, 99-103.

Woods, C. G., Bond, J. and Enard, W. (2005). Autosomal recessive primary microcephaly (MCPH): a review of clinical, molecular, and evolutionary findings. *Am. J. Hum. Genet.* **76**, 717-728.

Xie, Y., Jüschke, C., Esk, C., Hirotsune, S. and Knoblich, J. A. (2013). The phosphatase PP4c controls spindle orientation to maintain proliferative symmetric divisions in the developing neocortex. *Neuron* **79**, 254-265.

Supplementary Information

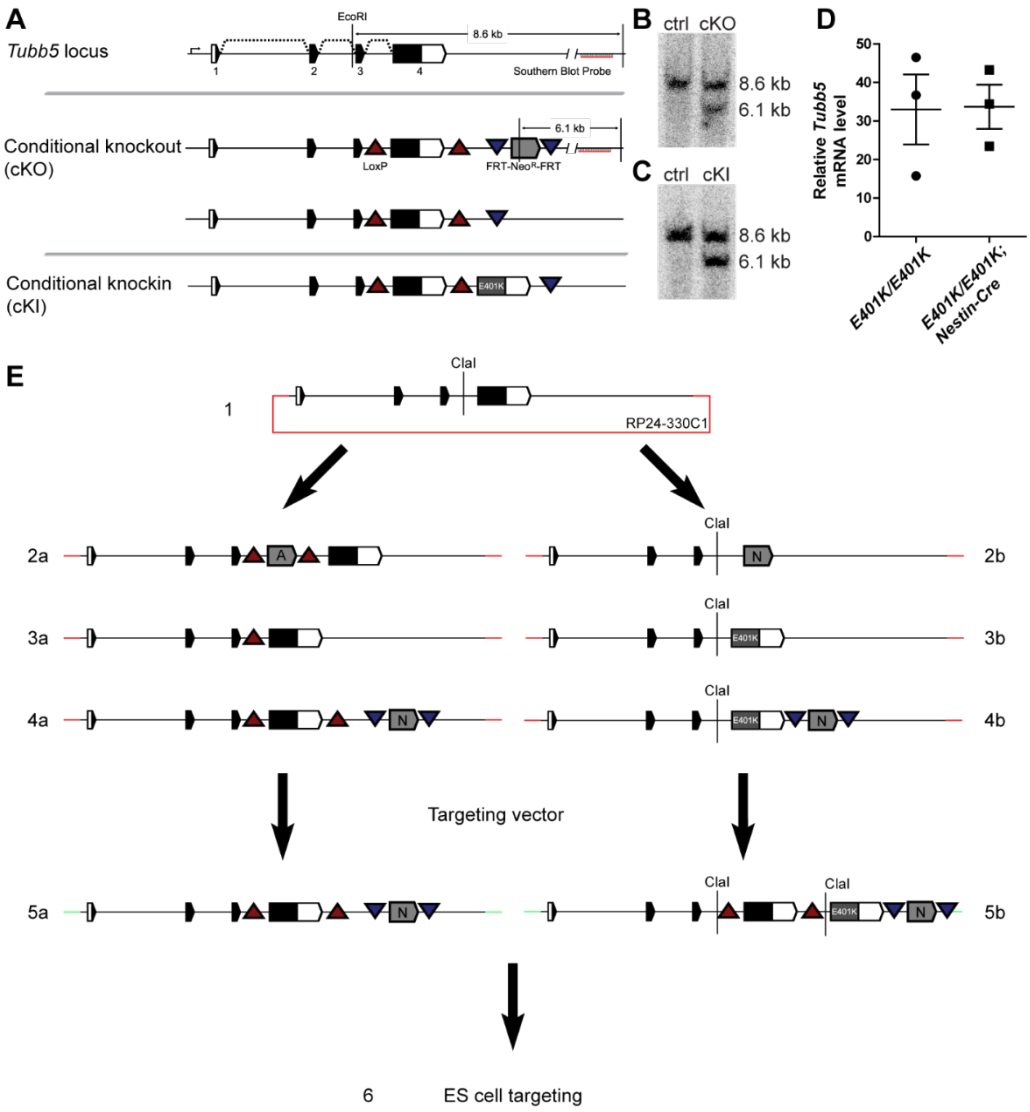

Fig. S1. (A) Schematic representation of the *Tubb5* locus, the conditional knockout allele before and after Flp- and Cre-recombination, and the conditional knockin allele. (B) Southern blot analysis of an ESC clone harboring the conditional knockout allele (ctrl=control, cKO=conditional knockout). (C) Southern blot analysis of an ESC clone harboring the conditional knockin allele (cKI=conditional knockin). (D) Quantification of the relative mRNA level of Tubb5 transcript, assessed in the embryonic cortex of *Tubb5(E401K/E401K)* and *Tubb5(E401K/E401K); Nestin-Cre* at E14.5. Homozygous knockin of the E401K mutation does not decrease transcript abundance. For the statistical analysis we employed a two-tailed Student's t-test. (E) Schematic representation of the generation of the two targeting constructs. Recombineering employed a BAC clone containing the *Tubb5* murine locus (RP24_330C1, 1). For the knockout, a LoxP-AmpR-LoxP (GeneBridges) construct was added upstream of Exon 4 (2a). Following Cre-recombinase mediated removal of the AmpR cassette (3a), a LoxP-FRT-NeoR-FRT cassette was added downstream of Exon4 (4a). For the knockin, Exon 4 was replaced by a NeoR cassette (2b) which was replaced by an E401K containing Exon 4 using negative selection (3b) followed by the addition of a NeoR cassette (4b). Both constructs were then transferred into the targeting vector. Utilizing an endogenous ClaI site a floxed version of Exon 4 (wild type) was added upstream of the mutated Exon 4 (5b). Targeting constructs (5a and 5b) were then used to target the endogenous *Tubb5* locus of ES cells (6).

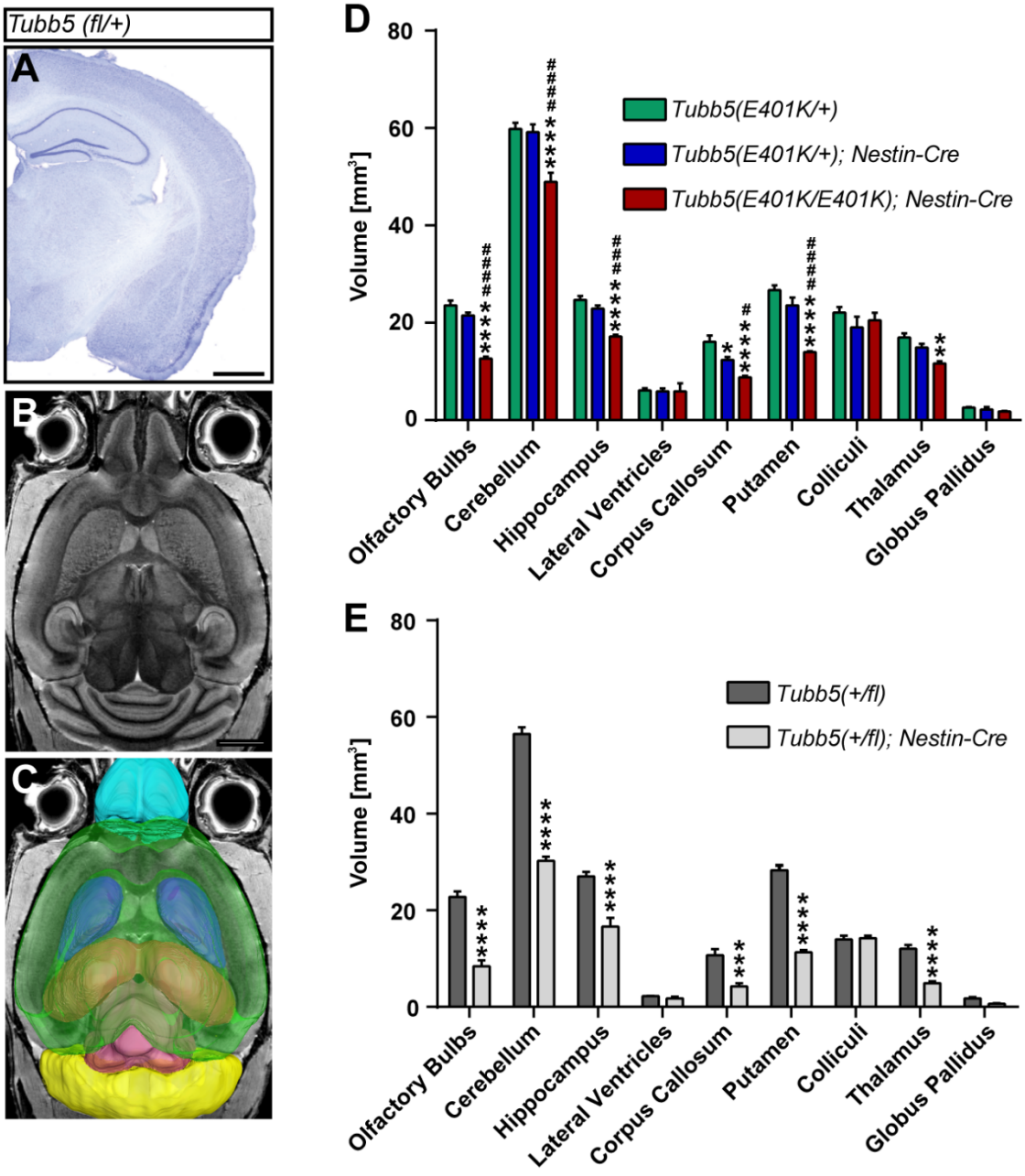

Fig. S2. Related to Fig. 1. (A) Nissl-stained, coronal section of the adult brain for *Tubb5(fl/+)*. (B) Axial magnetic resonance image (MRI) of a *Tubb5(fl/+)* mouse. (C) Same image as in B with 3D reconstructions of sampled brain regions following segmentation. Shown are olfactory bulbs (light blue), putamen (dark blue), hippocampus (red), cerebellum (yellow), the colliculi (light red) and the cortex (translucent green). (D-E) Quantifications of brain regions for the knockin (D) and knockout (E) mouse lines. Error bars show ± SEM. $*^{/\#}$P<0.05, $**^{/\#\#}$P<0.01, $***^{/\#\#\#}$P<0.001, $****^{/\#\#\#\#}$P<0.0001 (* and # in E indicate significance relative to *Tubb5(E401K/+)* and *Tubb5(E401K/+); Nestin-Cre*, respectively); for the statistical analysis shown in D-E we employed a two-way ANOVA with a Bonferroni post-test for multiple comparisons. Scale bars in A and B show 1000 µm and 2000 µm, respectively. n=3 for all conditions.

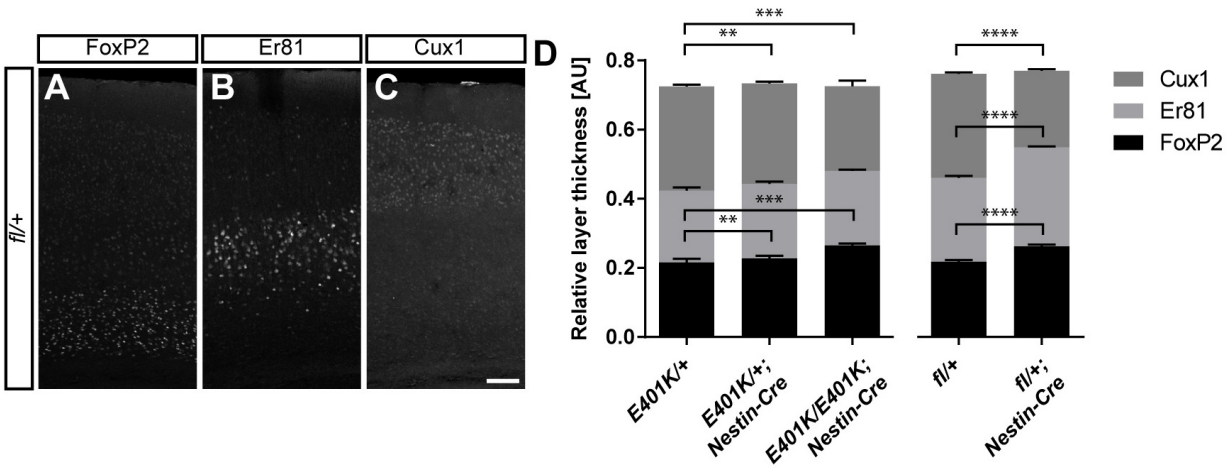

Fig. S3. Related to Fig. 2. (A-C) Control immunostaining of the *Tubb5(fl/+)* line for FoxP2 (A), Er81 (B) and Cux1 (C). These are littermate controls of the *Tubb5(fl/+); Nestin-Cre* animals show in Figure 2 (D, H, and L). (D) Relative cortical layer thickness for the knockin and knockout lines for FoxP2, Er81 and Cux1 positive layers. Graphs show mean ± SEM. **P<0.01, ***P<0.001, ****P<0.0001; for the statistical analysis shown in D we employed a two-way ANOVA with a Bonferroni post-test for multiple comparisons. Scale bar in C shows 100 µm. n=3 for all conditions.

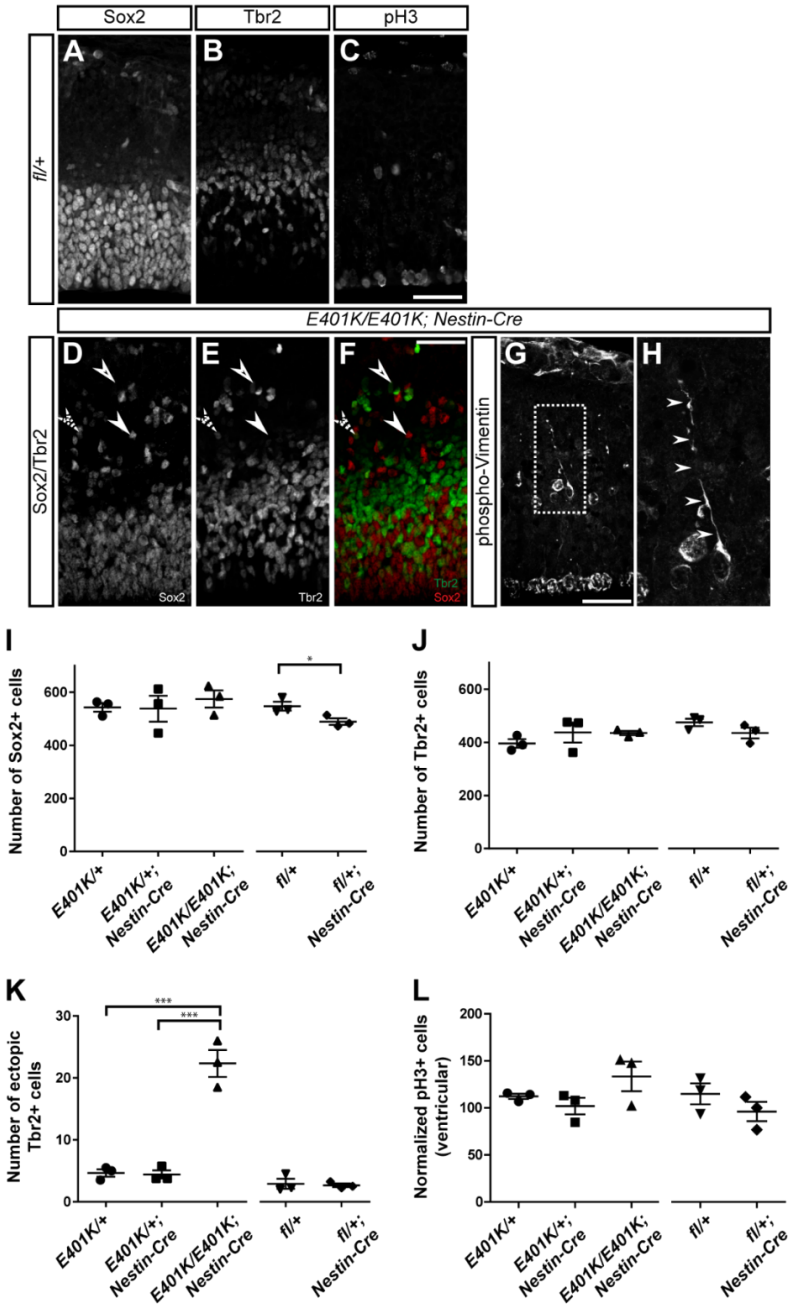

Fig. S4. Related to Fig. 3. (A-C) Immunostainings for Sox2 positive radial glial cells (A), Tbr2 positive intermediate progenitors (B) and pH3 positive mitotic cells (C) for the *Tubb5(fl/+)* embryonic cortex at E14.5. These are littermate controls of the *Tubb5(fl/+); Nestin-Cre* animals show in Figure 3 (D, H, and l). (D-H) Immunostainings for the *Tubb5(E401K/E401K); Nestin-Cre* embryonic cortex (E14.5) for Sox2 and Tbr2 (D-F) and phospho-Vimentin (G-H). D and E show grayscale images of F for Sox2 and Tbr2, respectively. Arrowheads in D-F indicate Tbr2 (open), Sox2 (closed) and double positive cells (open, dashed). G shows a phospho-Vimentin positive cell with a glial process and morphology consistent with an ectopic radial glial cell. H shows a magnification of the boxed region in G. Arrowheads indicate a putative basal process. (I-L) Quantification of the number of Sox2 positive (I), Tbr2 positive (J), Tbr2 positive ectopic (K), and the relative number of ventricular pH3 positive (L) cells for all genotypes. Error bars in I-L show the mean ± SEM. *P<0.05, ***P<0.001; for the statistical analysis shown in I-L we employed a one-way ANOVA with a Bonferroni post test for multiple comparisons for the knockin and a two-tailed Student's t-test for the knockout. Scale bars in C, F and G show 50 µm.

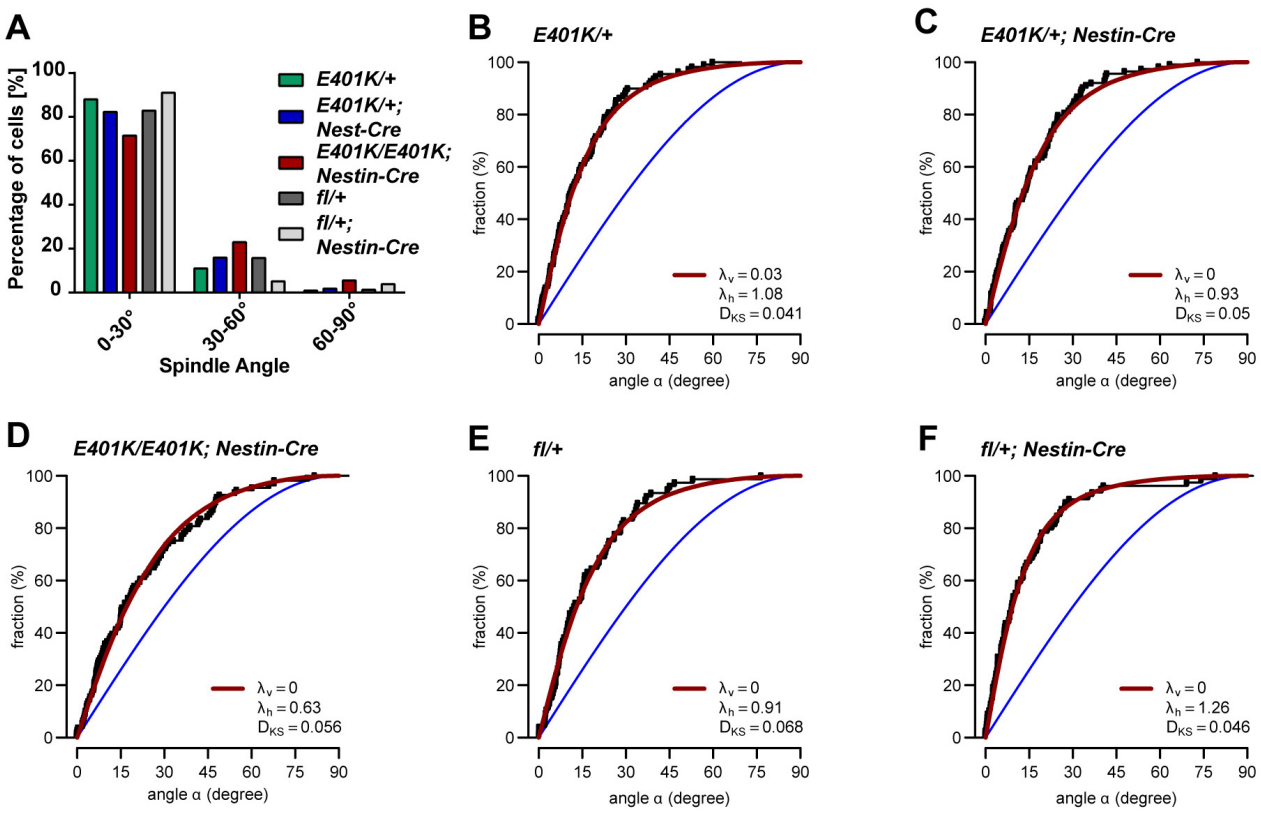

Fig. S5. Related to Fig. 3. (A) Quantification of the relative abundance of horizontal (0-30º), oblique (30-60º) and vertical (60-90º) spindle orientations for knockin and the knockout lines. Note the increase in oblique and vertical spindle orientations in the homozygous knockin (n=4 animals, n≥76 mitotic cells per condition). (B-F) Cumulative spindle angle plot for the data shown in A (1). λ_v and λ_h show enrichment for vertical and horizontal spindle orientations, respectively.

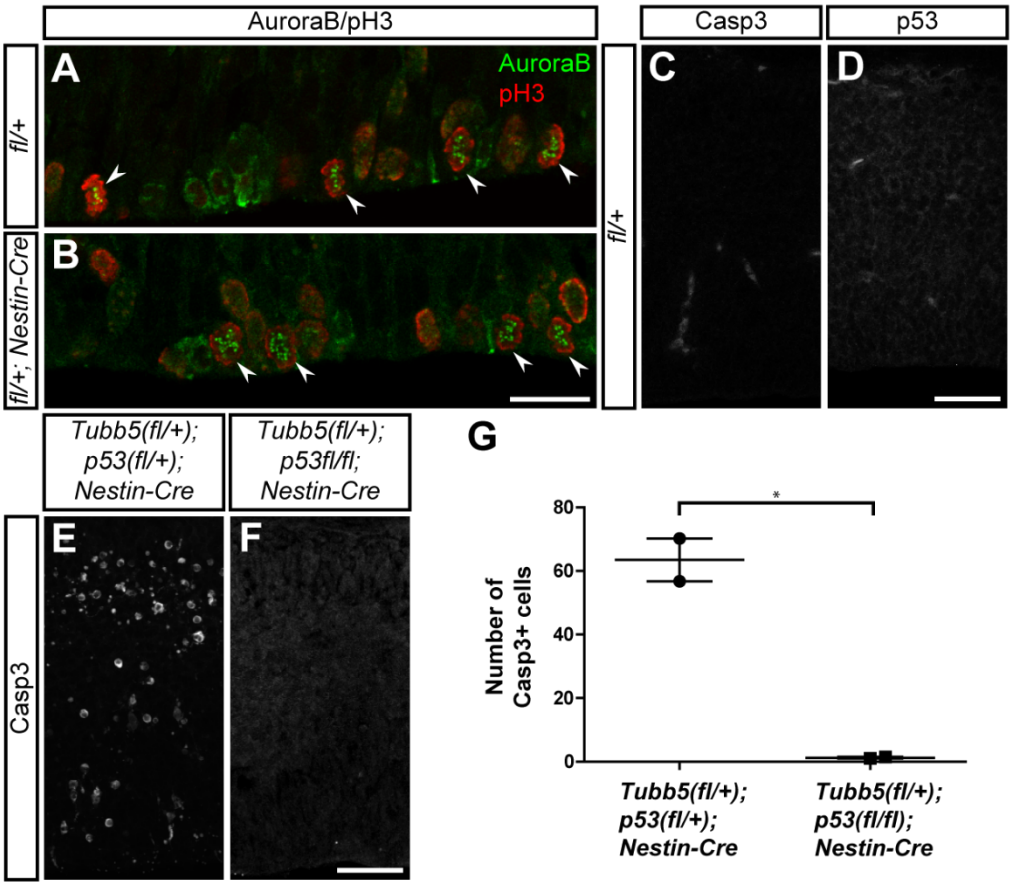

Fig. S6. Related to Fig. 4. (A-B) Immunstainings for AuroraB and pH3 for the heterozygous knockout line. Arrowheads indicate cells that were scored to be in metaphase. (C-D) Immunostainings for cleaved Caspase3 (C) and p53 (D) for the *Tubb5(fl/+)* embryonic cortex at E14.5. These are littermate controls for the data shown in Figure 4T and X. (E-F) Immunostainings for cleaved Caspase 3 for a *Tubb5(fl/+); p53(fl/+); Nestin-Cre* embryonic cortex at E14.5 and a *Tubb5(fl/+); p53(fl/+); Nestin-Cre* rescue. Note the absence of cleaved Caspase3 staining upon homozygous knockout of p53. (G) Quantification of the number of cleaved Caspase 3 positive cells for the genotypes shown in E and F. Error bars in G show the mean ± SEM. *P<0.05; for the statistical analysis shown in G we employed a two-tailed Student's t-test. Scale bars show 50 µm in D and F and 20 µm in B. n=3 for A-D; n=2 for E-G.

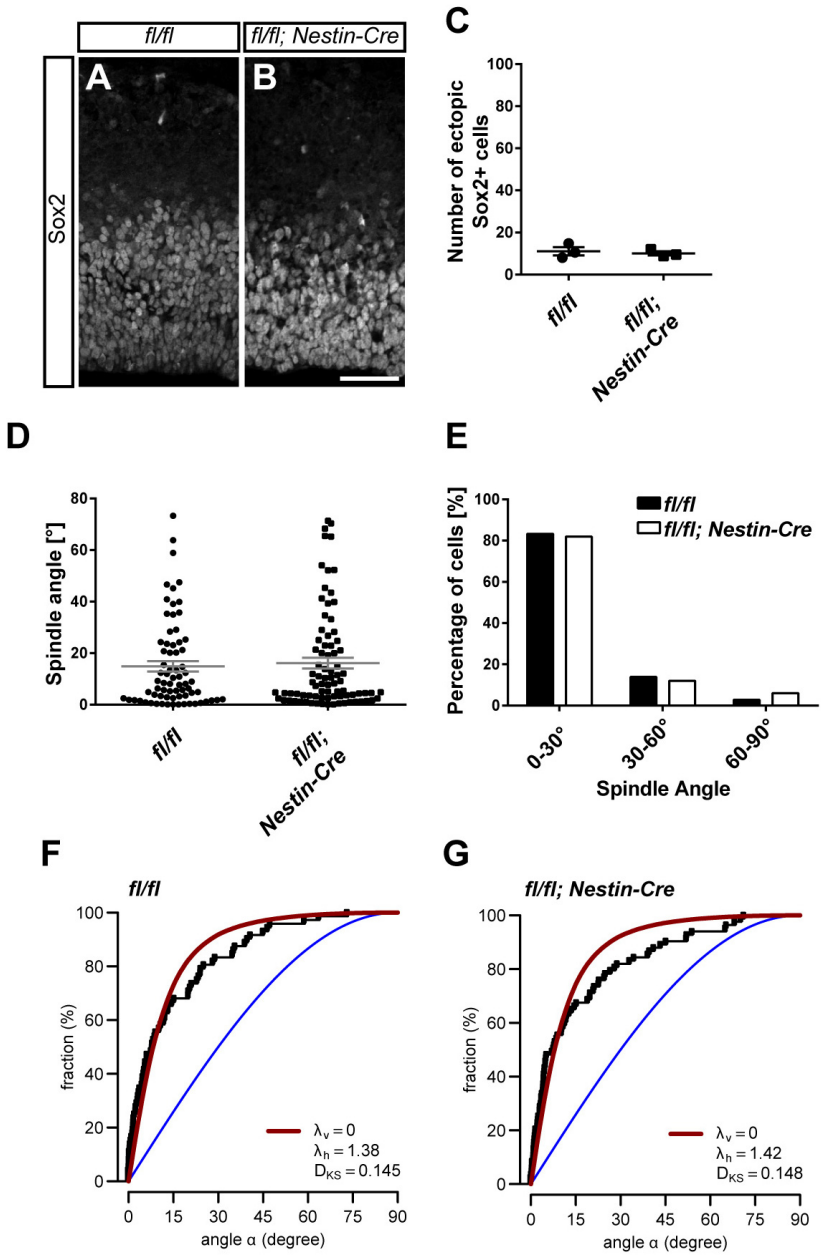

Fig. S7. Related to Fig. 5. (A-B) Immunostainings for the radial glia marker Sox2 for the homozygous knockout (*Tubb5(fl/fl); Nestin-Cre*) and a littermate control (*Tubb5(fl/fl)*). (C) Quantification of the number of ectopic Sox2 positive cells found per cortical image. (D-E) Quantification of spindle angle measurements for the homozygous knockout and littermate controls. There is no significant difference in average spindle orientation. Graphs show the summary of the total population of cells analyzed (n=3 animals, n≥72 mitotic cells per condition). (F-G) Cumulative spindle angle plot according to Jüschke and colleagues for the data shown in A and B (1). Error bars in C and D show ± SEM. For the statistical analysis shown in C-D we employed a two-tailed Student's t-test. Scale bar shows 50 µm in *B*.

Table S1. Primers

Tubb5_LoxP_F	TCTAGAACCTGGGACTATGG
Tubb5_LoxP_R	CACCACATCCAAGACAGAG
Cre_F	TCGCGATTATCTTCTATATCTTCAG
Cre_R	GCTCGACCAGTTTAGTTACCC
Tubb5_SB_F	CGGTGGCTTACTCTTAAGACTG
Tubb5_SB_R	CTTGAGTCATGGCTGGGGAG
Southern Blot Probe	CGGTGGCTTACTCTTAAGACTGgcagcaaagacaaatggagacatgtgaacaggactgcggag gtagattatgaccacaaagggctcagtgccctcgggaccctcatactgtagcgacttacccagggagggcaagtacc agcctcatccattctgacgctaagtccttagcctagctgctctaagaagtcacaaggcggttcccaggccctggcttgat tctgtgcctgaaatggatcccactaccgagtaggctgagctgaccagaagaatgcttcctgggtctcttccacgttgtgt atcccactggtggcgctggcttttctctctgactcaggccacccgCTCCCCAGCCATGACTCAAG

Table S2. Antibodies

Antibody	Supplier	Dilution	Blocking solution
FoxP2	Abcam (ab16046)	1:500	0.1% TX-100/PBS; 2% ds
Er81	Kind gift of the Jessel laboratory	1:3000	0.3% TX-100/PBS; 2% ds
Cux1	Santa Cruz (sc-6327)	1:100	0.1% TX-100/PBS; 2% ds
Sox2	Santa Cruz (sc-17320)	1:200	0.3% TX-100/PBS; 2% ds
Tbr2	Abcam (ab23345)	1:200	0.3% TX-100/PBS; 2% ds
Dcx	Santa Cruz (sc-8066)	1:100	0.3% TX-100/PBS; 2% ds
pH3	Millipore (06-570)	1:500	0.3% TX-100/PBS; 2% ds
N-Cadherin	Invitrogen (3B9)	1:500	0.3% TX-100/PBS; 2% ds
γ-Tubulin	Sigma-Aldrich (T6557-.2ML)	1:100	0.3% TX-100/PBS; 2% ds
p-Vimentin	MBL (D-076-3)	1:1000	0.3% TX-100/PBS; 5% BSA
Cleaved Casp3	Cell Signaling (9661S)	1:400	0.3% TX-100/PBS; 2% ds
p53	Leica Microsystems (P53-CM5P)	1:1000	0.3% TX-100/PBS; 2% ds
AuroraB	BD Biosciences (611083)	1:250	0.3% TX-100/PBS; 2% ds